Article

Smart Self-Sensing Piezoresistive Composite Materials for Structural Health Monitoring

Relebohile George Qhobosheane [1,2], Monjur Morshed Rabby [1,2], Vamsee Vadlamudi [2], Kenneth Reifsnider [1,2] and Rassel Raihan [1,2,*]

1   Department of Mechanical and Aerospace Engineering, School of Engineering, University of Texas at Arlington, Arlington, TX 76019, USA; relebohile.qhobosheane@mavs.uta.edu (R.G.Q.); monjurmorshed.rabby@mavs.uta.edu (M.M.R.); kenneth.reifsnider@uta.edu (K.R.)
2   Institute for Predictive Performance Methodologies, University of Texas at Arlington Research Institute, Fort Worth, TX 76118, USA; vamsee.vadlamudi@uta.edu
*   Correspondence: mdrassel.raihan@uta.edu

Abstract: The use of fiber-reinforced composite materials has widely spread in various sectors, including aerospace, defense, and civil industry. The assessment of these heterogeneous material systems is important for safer and risk-free applications and has contributed to the need for self-sensing composites. This work is focused on the development of piezoresistive composites, the prediction of their performance and structural health monitoring (SHM). Additionally, this work unpacks the complexity of carbon nanotubes (CNTs) micro-fabrication and the development of piezoresistive and electromagnetic (EM) waves detection electrodes. Scanning electron microscopy (SEM) was used to characterize the CNTs structure and morphologies. The manufactured CNTs were incorporated in epoxy systems to fabricate glass fiber reinforced polymer (GFRP)-CNTs smart composites with piezoresistive properties. The detection of micro-damage onset and its progression was carried out in mode I, to evaluate the sensitivity of the smart composites to damage development. The change in electrical conductivity of the nanotubes-reinforced composite systems due to localized mechanical strains enabled crack propagation detection. The relationship between crack propagation, fracture toughness, and electrical resistivity of the smart composite was analyzed.

Keywords: piezoresistive; carbon nanotubes; mechanical and piezoresistive properties; crack propagation; fracture toughness; electrode sensitivity

1. Introduction

Advancements in materials research have led to the development of smart materials. This is seen in different applications, which include sensors, structural materials, and actuators, among others [1–3]. This work focuses on the development of piezoresistive smart self-sensing composites for structural health monitoring (SHM). The piezoresistive property in these composites is attained from the use of carbon nanotubes (CNTs). All CNTs fabricated in this work followed the chemical vapor deposition (CVD) method to develop single-walled carbon nanotubes (SWCNTs) and multi-walled carbon nanotubes (MWCNTs). The integration of these CNTs into composite materials can improve mechanical properties and electrical resistivity. Current advances in piezoresistive CNTs-based composites have been reported in reference [4], which explores the contribution of oriented nickel-coated carbon nanotubes to the improvement of conductivity and piezoresistive property of cement-based composites. This study found that nickel-coated carbon nanotubes cement-based composites oriented parallel to the magnetic field direction have the best piezoresistive characteristics under cyclic compressive loading. Wang et al. [5] investigated the piezoresistive behavior of carbon nanotube composite films subjected to lateral compressive strain. The effects of the matrix type, functionalization, and acid treatment on the piezoresistive response of CNT composite films were investigated in this study. The

modulus of composite films was discovered to have a significant impact on their piezoresistive response. Stronger interfacial bonding was also shown to improve the piezoresistive response and the gauge factor associated with it. MWCNT epoxy-based piezoresistive films are also explored by Sanli et al. [6]. Digital image correlation was used to examine the deformation over the piezoresistive films area under quasi-static uniaxial tension and the piezoresistive features of the films. Higher sensitivity was obtained in comparison to typical strain gauges, particularly at concentrations around the percolation. A non-linear piezo-resistivity was discovered at low concentrations due to the tunneling effect. The study reported in [7] also shows a comparison of the SHM performance of CNT-based piezoresistive composites versus conventional SHM approaches. The goal of the study was to investigate the piezoresistive performance of MWCNTs/epoxy nanocomposite under uniaxial cyclic tensile and compressive loading in the low strain region. After cyclic loading and unloading, the strain-sensitive nanocomposite showed remarkable performance, including a gauge factor of up to 78, good stability, and durability. Sabagh et al. [8] integrated carbon nanofibers and MWCNTs into glass fiber reinforced polymer (GFRPs) composites at various volume fractions. The fabricated specimen conductivity response with changing volume fraction was characterized to monitor moisture-induced damage propagation [8]. In another study, Zhou et al. [9] used ultrasonic cavitation to infuse CNTs into an epoxy system with a weight fraction of 0.3 percent. This contributed to the material piezoresistive property used to monitor fracture toughness. The detection of the piezo-resistivity of a CNT-embedded composite showed to respond to the overall damage of the composite and not the isolated crack location.

During the fracture process, high concentration of energy spikes within a small volume of material lead to emission of particles, i.e., electrons, ions, and neutral species, as well as photons from the surfaces both during and after crack propagation, called fracto-emission (FE) [10]. In this work, electromagnetic (EM) waves emitted at the propagating crack tip were monitored. When an atomic particle, such as an electron, is accelerated by an electric field and moves, electromagnetic waves are produced. The movement produces oscillating electric and magnetic fields that travel at right angles to each other. The variation of EM waves due to the addition of nanoparticles has not been widely explored by researchers unlike structural health monitoring using EM waves [10–13]. The application of EM waves for structural health monitoring (SHM) has been examined in the literature [14] where crack generated at the bend of a pipe is characterized by high frequency electromagnetic waves excited using a network analyzer. The variation in crack propagation was monitored in the reflected back EM waves signal. The release of EM waves during loading of specimens like rocks was explored in [15]. The study showed how EM waves are generated during crack propagation and the variation in EM waves during different type of loadings. This technique is applied in this work to monitor the change in EM waves released in composite with and without CNTs, following the novel approach that correlates EM waves with composite resistivity during loading. However, in various studies, fiber Bragg grating sensors (FBG) were used to evaluate the crack growth in fiber-reinforced polymers [16]. When using FBG sensors embedded in fiber-reinforced polymers, there is a serious risk of the sensor being damaged. The signal decreases if the crack changes the direction of travel and traverses the optical fiber [16]. Electrical resistivity measurements have also been used in the literature for crack detection and propagation during flexural loading [17]. The main disadvantage of this method is the unstable electrical resistivity signal; to address this issue, researchers used different coating [18] or improved adhesion between the probes and the specimen [19]. The initial phase of this work is focused on the fabrication of carbon nanotubes and the composite. The next phase consists of the development of the detection methodology, and then the testing and characterization of the CNTs-based piezoresistive composites in comparison to epoxy-based composites without CNTs during crack propagation.

2. Materials and Methods

The fabrication of CNTs and composite specimens is detailed in this section. First, the physical vapor deposition method used for the catalyst deposition is described. Next, the CVD parameters and steps followed in synthesizing the CNTs are described. The integration of the fabricated CNTs with glass fiber reinforced (GFRP) composites is explained together with the fabrication methods of the electrodes for the detection of EM waves and the measurement of the electrical resistivity. In this experiment, 105B epoxy resin with the 207SB epoxy hardener from West Systems, Bay City, MI, United States of America was used for making the Epoxy/glass fiber composite. All the characterization methods used are also described in this section, including mechanical testing techniques.

2.1. Specimen Preparation

The first step in the fabrication of testing specimens in this work was the preparation of the catalyst for growing carbon nanotubes. Physical vapor deposition [20] was used for the deposition of solid Nickel (Ni) catalyst on a silicon wafer. This was done by releasing Ni atoms into solid state and passing into the gas phase by bombardment with energetic ions during the sputtering process run in DC. Subsequent steps included the synthesis of carbon nanotubes using the prepared catalyst. The process was carried out using an in-house PLANAR-Tech CVD deposition system by PLANAR-Tech, The Woodlands, TX, United States of America [21]. The type of CNTs fabricated in chemically extracted carbon atoms by catalytic decomposition of precursors depended on various parameters such as catalyst, temperature, and others. Before running the CVD nitrogen, argon, and hydrogen gases and acetylene as a carbon source were turned on. The CNT growth process was carried out inside a quartz tube within a single-zone furnace able to withstand high temperatures, as shown in Figure 1.
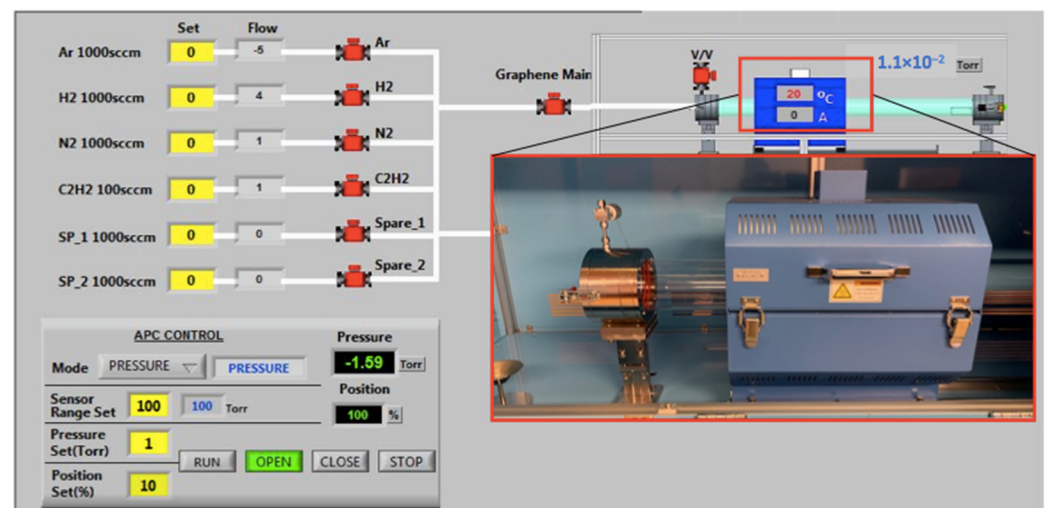

Figure 1. Chemical vapor deposition setup for carbon nanotube fabrication.

The chamber was sealed with gas to avoid CNTs etching from the substrate after fabrication. Acetylene was then let into the chamber at 1000 °C onto the substrate sputtered with Ni catalyst for the period of time necessary to grow CNTs. This is an endothermic reaction [22] with high temperature affecting the reaction kinetics and accelerating the decomposition rate of the carbon precursor. For the growth of SWCNTs and MWCNTs, changes to the fabrication recipe were made. SWCNTs were made at lower temperatures of 800 °C with smaller catalyst particle sizes, whereas MWCNTs were synthesized at 1000 °C with substantially larger catalyst particle sizes. This process was highly dependent on the temperature and flow rate as at temperatures that are too high, the CNT growth reaction stops and results in a non-reactive catalyst. Upon completion of CNTs growth, an inert gas

was flushed into the quartz tube and temperature cooled down to 200 °C and less. The van der Waal forces in CNTs cause them to cluster together. The aggregation of carbon nanotubes was avoided in this study by functionalizing the CNTs in acid. Following exohedral functionalization, 50 mg of CNTs were dispersed in 150mL of 1:3 HNO_3: H_2SO_4 solution and agitated at 500 rpm at 120 °C. Deionized (DI) water was utilized to properly clean the CNTs after they had been acid-treated [3]. The manufactured nanotubes were sonicated in ethanol using a Branson Sonifier S-250D with a 13 mm end cap diameter having a cylindrical tip to enhance their solubility and then added to a West System 105B epoxy resin with the 207SB epoxy hardener. The solution was vacuum run between 8 plies of glass fiber during the process of vacuum-assisted resin transfer molding (VARTM) and allowed to cure for 24 h. A resin and hardener ratio of 1:0.22 has been used to make the composite. The fiber volume fraction has been kept at 50–60%. The fabricated composite specimens were then cut into the required dimensions as per mode I ASTM D5528 tests [23] for the mechanical tests. A concentration of 0.34 wt.% CNTs was used in the resin system based on previous research [3]. Vertuccio et al. investigated the sensing property of 0.3 wt. percent MWCNT embedded epoxy resin. According to that research, the addition of CNT (in the range of 0.1–0.3% wt.) to the resin system increases the electrical conductivity when compared to pure resin [24]. Rather et al. also dispersed 0.1% wt. of MWCNTs into the resin for fabricating the composite, and they found a 32.8% increase of the maximum flexural strength over normal epoxy glass fiber composites [25]. So, the concentration of CNT in the range of 0.1–0.3% wt. increase both mechanical and electrical property of the epoxy/fiber composite [25].

2.2. Electrodes Fabrication

The design and selection of the electrode material used to measure the electrical property [26] was based on the application requirements. The electrode was required to be flexible and possess high electrical conductivity. Copper (Cu) was selected for the electrode because of its excellent properties, which include direct current electrical conductivity of 5.96×10^7 Sm^{-1} [27]. The sample was sandwiched between the two electrodes, which were wired into an alpha analyzer (broadband dielectric spectroscopy) that measured the sample's resistivity. The impedance of the sample was measured after it was subjected to an AC electric field. The resistance component R of the impedance $Z^* = R + iX$, where X = reactance, was then isolated and plotted against the crack opening length. The detection system of electromagnetic waves was based on the changes in magnetic and electrical components near the surface of the crack. The detection device and amplification were designed for micro-cracks in composite specimens as a source of EM waves. EM waves from crack propagation were picked up by a conductive wire element placed in proximity to the specimen's crack area. To amplify the signal, JFET amplifier was connected to this system. A common source amplifier was designed with a self-biasing scheme that could pick up a signal with a target voltage gain of 6 amplifying signal. The amplifier circuit diagram is shown in Figure 2.

To select the parameters for this circuit, a test circuit with a JFET transistor was initially setup and a voltage gate to source was swept in 50 mV steps to determine the drain current at each step. This therefore led to the trans conductance (qm) plot where the q point was set from mid low to high current and both qm and source resistance R_s were calculated from the slopes as shown in Figure 3.
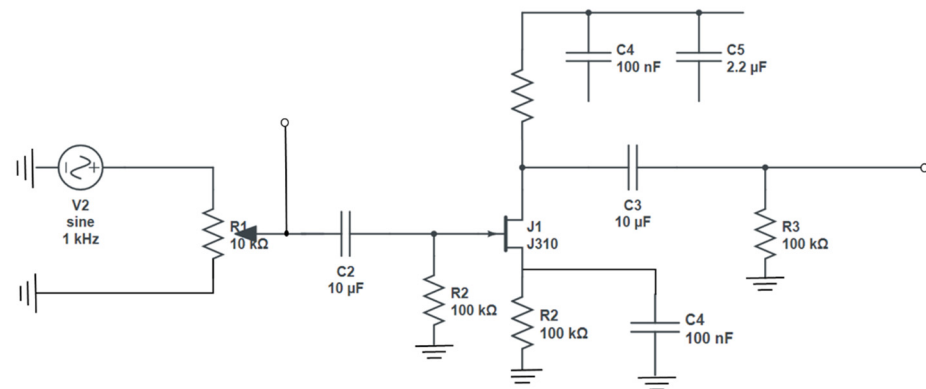
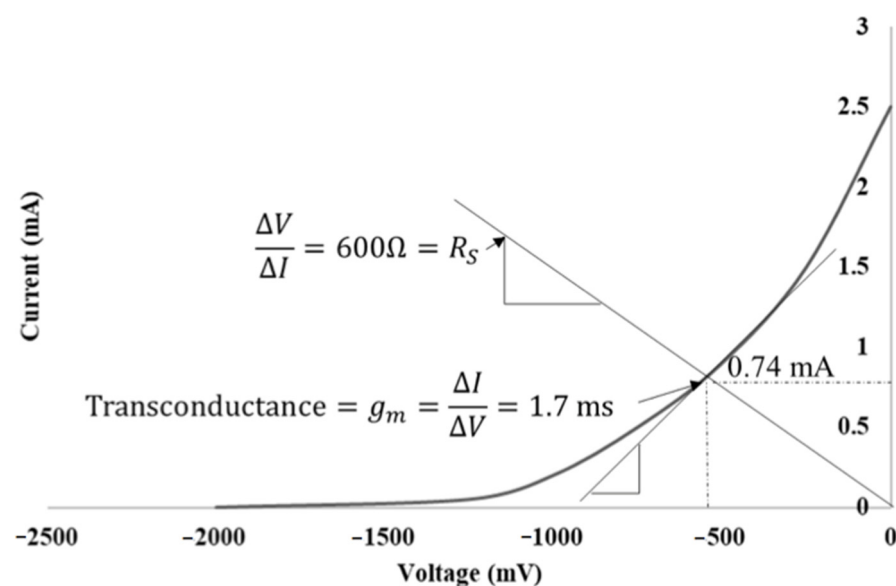**Figure 2.** Circuit diagram for the JFET amplifier used in this work.

Figure 3. Transconductance curve for the FET to determine source resistance.

The trans conductance was therefore used to determine the drain resistance for the circuit to a value of approximately 3.6 kΩ. This system was sensitive to any conductive materials; therefore, a Faraday cage was designed for all specimens tested in this work. The amplified signal was then transferred to an oscilloscope for further analysis. Piano hinges were connected to each fabricated composite specimen on one end with a pre-generated crack that represents separation during loading. Each end of the piano hinge was clamped by the micro tensile testing machine used in this work. The mode I test was conducted within a Faraday cage, as shown in Figure 4. To enable crack propagation in the mode I test, the stress was applied normally to the plane of the crack. The critical strain energy release determined the crack propagation through these composite specimens and was dependent on the crack separation displacement, specimen width, initial crack length, the load, and the correction factor. The conductive area of the fabricated CNT-GFRP specimens decreased as the fracture spread through the specimens during loading, resulting in an increase in the through thickness electrical resistance. It should also be noted that the measurement is through-thickness, which means that the setup is similar to a parallel plate capacitor, as shown in the inset of Figure 4. This setup was used because we are attempting to measure change in resistivity with propagation of an interlaminar crack, which is a through thickness effect that is more sensitive to changes than in-plane measurements. In this paper, the variations in electrical resistance that occurred during incremental crack growth are presented. During broadband dielectric spectroscopy (BbDS) experiments,

the electrical resistance R was measured using the two-electrode method at the 100 Hz frequencies. The normalized resistance change ($\Delta R / R_0$.) was therefore determined by

$$\frac{\Delta R}{R_0} = \frac{R - R_0}{R_0} \tag{1}$$

ere the initial resistance recorded before loading the specimen is represented by R_0. From this formulation, the predicted changes in electrical resistance as a function of the separation increase were calculated. The gauge factor was not calculated in this work since it is dependent on the change in specimen length with respect to initial length, and this work focused only on the mode I, which measured the gap of the crack opening length. Therefore, the data reflected in the results section from resistivity and EM waves detection experiments were correlated with separation as the load was increased to monitor crack behavior. The initiation and propagation of delamination in all fabricated composite samples followed the ASTM D5528.
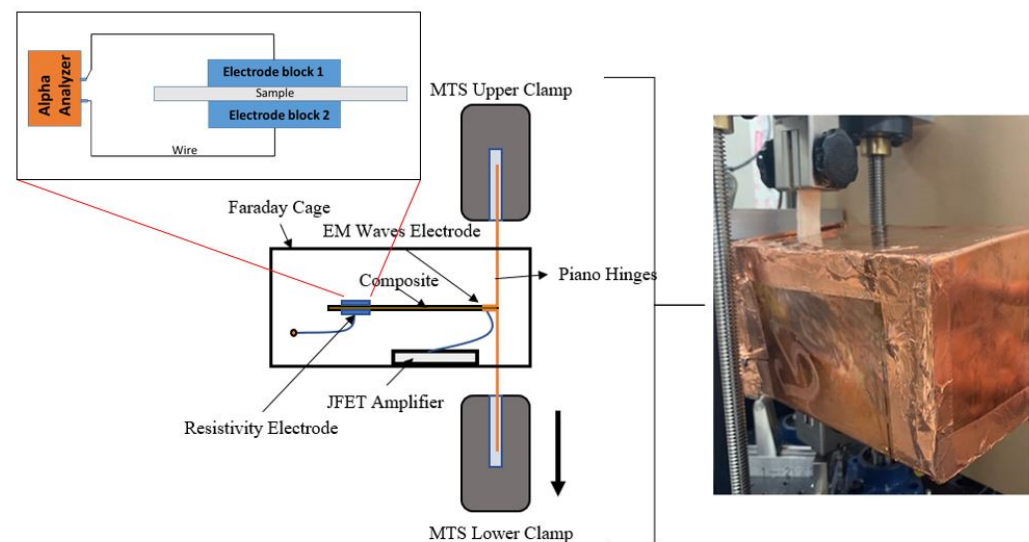

Figure 4. Mechanical testing setup for all composite specimens in this work.

2.3. Characterization and Testing

The first step in our characterization was the analysis of the fabricated CNTs using Fourier Transform Infrared Spectroscopy (FTIR) and Differential Scanning Calorimetry (DSC). FTIR (Nicolet™ iS50 by Thermo Fisher Scientific, Waltham, MA, USA) was used to characterize both multi-wall and single wall carbon nanotube. All scans were taken in transmission mode at a resolution of 4 cm^{-1}. The measurements were taken at wavenumbers ranging from 4000 cm^{-1} to 650 cm^{-1}. For the collection of the spectra, an Attenuated Total Reflection (ATR) module has been used to measure the changes in an IR beam that is reflected internally when the beam comes in contact with a specimen. Absorption data for all samples was therefore acquired. DSC was used to measure the thermal properties of the carbon nanotube. The DSC thermograph depicts the difference in heat flow between the sample and the reference [28]. In this experiment, DSC 25 from TA instrument (New Castle, DE, USA) is used to carry out all the tests. The sample weights are maintained from the range of 5–15 mg. A standard copper pan was used due to high temperature operation. Tests at different heating rates of 5, 7 and 9 °C/min were carried out from room temperature to 725 °C and the data were later used in Kissinger and Ozawa kinetic equations to calculate the thermo-kinetic parameters. The morphology of all fabricated CNTs in this work was investigated using the scanning electron microscope (SEM) and results are detailed in the next sections.

3. Results and Discussion

This section describes the results attained from the fabricated samples and characterization of CNTs before fabrication. As stated in the Characterization and Testing section, the bonding and thermal properties of SWCNTs and MWCNTs were explored using FTIR and DSC, respectively. Figure 5 shows the absorption properties of the SWCNT, and Figure 5b presents the MWCNT fabricated in this work.
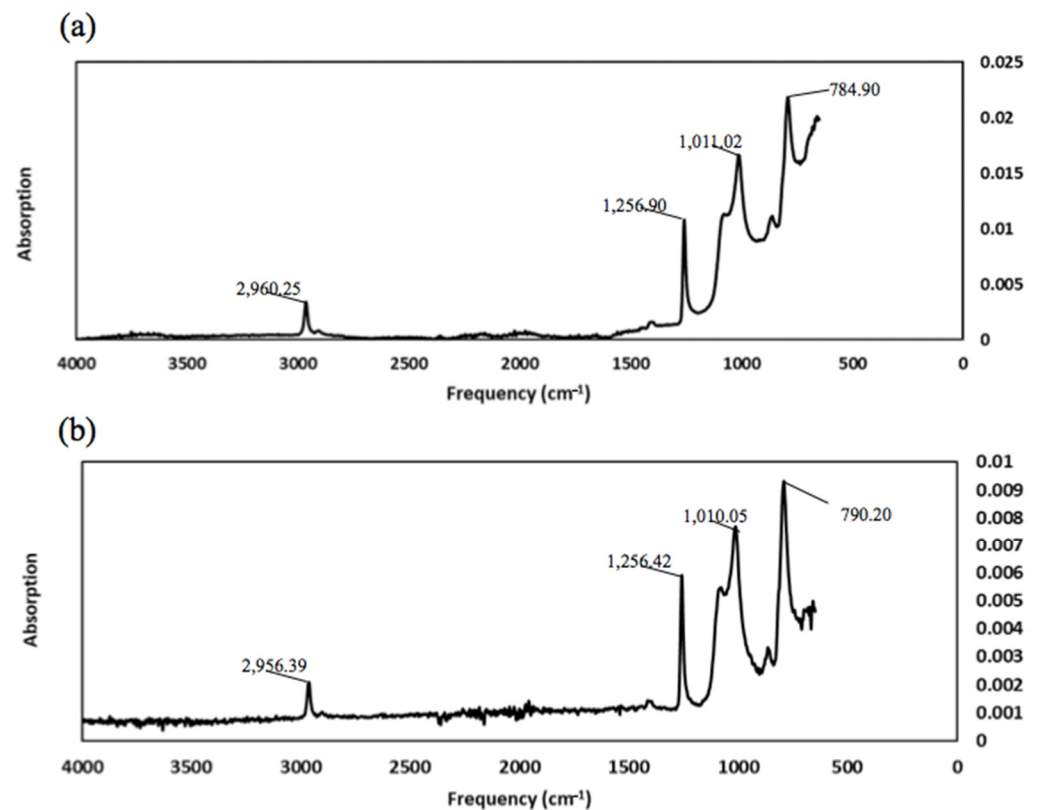

Figure 5. (**a**) The absorption properties of the SWCNT fabricated in this work and (**b**) the MWCNT fabricated in this work.

From the FTIR data shown in Figure 5, both SWCNT and MWCNT showed similar trends in absorption peaks. This is because both fibers are of the same material, the difference being the number of layers in MWCNTs. The presence of Si-O is observed at 1011.02 cm^{-1} for SWCNT and at 1010.05 cm^{-1} for MWCNT because a silicon wafer was used as a substrate during the fabrication process. At 1256.90 cm^{-1} and 1256.42 cm^{-1}, peaks due to C-O bonds are noted for SWCNT and MWCNT, respectively. These bond structures contribute to the crosslinking with epoxy during composite fabrication affecting the piezoresistive property of the composite. Peaks due to C-H bonds were also observed at 2960.25 cm^{-1} and 2956.25 cm^{-1} for both SWCNT and MWCNT, respectively. A slight difference was also observed at 790.20 cm^{-1} peak intensity of cis = C-H functional group in MWCNT being higher than that of SWCNT, which was at 784.90 cm^{-1}. The results of the thermal decomposition study for both SWCNT and MWCNT carried out in this work are shown in Figure 6.
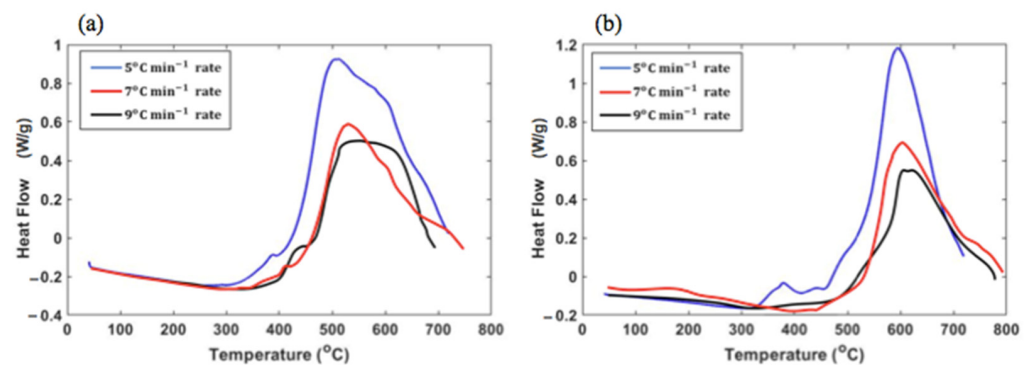
Figure 6. DSC results at different heating rates for (**a**) SWCNT and (**b**) MWCNT.

Each sample of nanotubes was characterized at three heating rates, 5 °C/min, 7 °C/min, and 9 °C/min. SWCNT samples showed lower peak temperatures at 511 °C when the heating rate was set to 5 °C/min compared to MWCNT with a peak at 591 °C. This peak was due to the thermal decomposition of the synthesized CNTs [29]. It was noted that for each sample, peak temperatures shifted with increasing heating rates. Using the peak temperature for different heating rates, the activation energy was calculated using both Kissinger and Flynn–Wall–Ozawa models [30,31]. The thermo-kinetic investigation was carried out to determine the amount of energy required for the carbon-oxygen reaction to take place. The thermo-kinetic study also allows for a comparison of the stability of the SWCNT and MWCNT, which were created in the lab using chemical vapor deposition. The Kissinger model is based on the equation [32]:

$$\ln\left[\frac{\beta}{T_m^2}\right] = \ln\left[\frac{ZR}{E}\right] - \frac{E}{RT_m} \qquad (2)$$

where the heating rate in °C/min is given by β, the temperature at peak maximum for each sample is given as T_m, and the ideal gas constant as R. The model is also dependent on the pre-exponential factor Z and the activation energy E. For each heating rate in Figure 7, Equation (2), which is in the form of $y = mx + c$, was used to generate a linear plot with x set as $(1000/T_m)$.
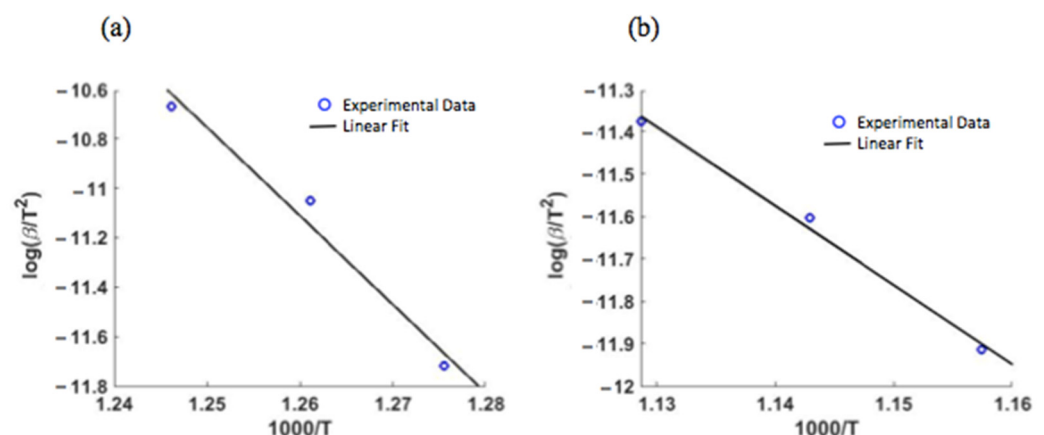

Figure 7. Kissinger data line for (**a**) SWCNT samples and (**b**) MWCNT samples. Blue circles indicate dataset derived from the peak temperature of the DSC thermograph, and the black line is linear fit of the experimental data.

The relationship between the activation energy and heating rate for both SWCNT and MWCNT is shown in Figure 7, where the slope of the curves represents the activation energies. This is due to the increase in nanotube layers in MWCNT samples. Further

characterization of the carbon nanotube samples using the Flynn–Wall–Ozawa model used equation [30]:

$$\log \beta = \log\left(\frac{AE}{g(\alpha)R}\right) - 2.315 - \frac{0.4567E}{RT} \tag{3}$$

The thermal degradation mechanism for each nanotube sample is represented by $g(\alpha)$ in the above formulation, where α is the fractional conversion. The linear fitting of $\log \beta$ against $1000/T$ for SWCNT and MWCNT is therefore shown in Figure 8.
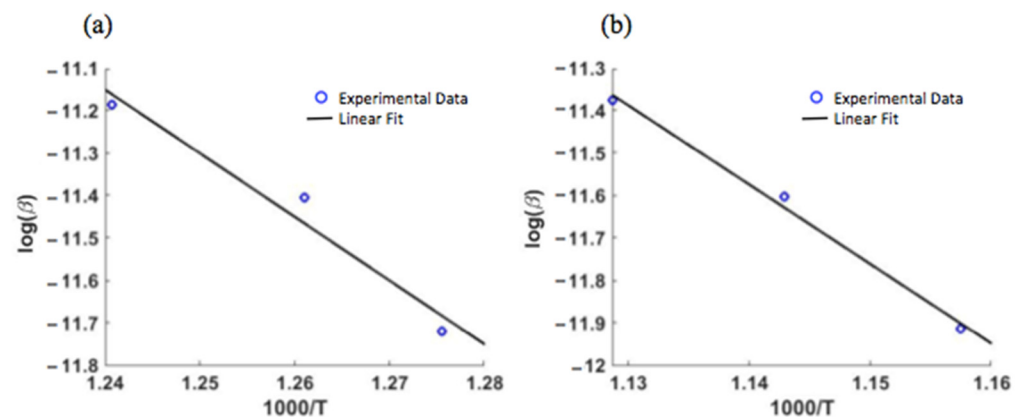

Figure 8. Flynn–Wall–Ozawa data line for (**a**) SWCNT samples and (**b**) MWCNT samples. Blue circles indicate dataset derived from the peak temperature of the DSC thermograph, and the black line is linear fit of the experimental data.

From the Flynn–Wall–Ozawa plot data for both SWCNT and MWCNT given in Figure 8, the activation energy can also be obtained from the slope, which was 131.102 kJ/mol for SWCNT and 161.725 kJ/mol for MWCNT. According to these findings, MWNTs are the most stable carbon forms. CNT-embedded epoxy went through a thermal curing cycle during the manufacturing process, which had a chemical effect on the CNTs. The thermo-kinetic analysis provided insight into the chemical changes (thermal decomposition) that occurred during the curing reaction of the CNT-embedded epoxy. The activation energy for the fabricated nanotubes was correlated to the mechanical and thermal properties of the composite samples. A slight increase in activation energy from 124.696 kJ/mol to 155.59 kJ/mol was observed from SWCNT to MWCNT samples, as shown in Table 1. This is consistent with the literature, as evidenced in [33].

Table 1. Activation energy calculations for SWCNT and MWCNT.

	Thermo-Kinetic Model				
Heating Rate (°C/min)	**5**	**7**	**9**	**Kissinger Activation Energy (kJ/mol)**	**Ozawa Activation Energy (kJ/mol)**
Peak temperature (SWCNT)	511	520	533	124.696	131.102
Peak temperature (MWCNT)	591	602	613	155.588	161.725

The morphology of the fabricated carbon nanotubes for both SWCNT and MWCNT was characterized using a scanning electron microscope (SEM), as shown in Figure 9. The diameter for both the SWCNT and MWCNT vary between 15 and 60 nm. The diameter dispersion was higher in SWCNTs shown in Figure 9a.
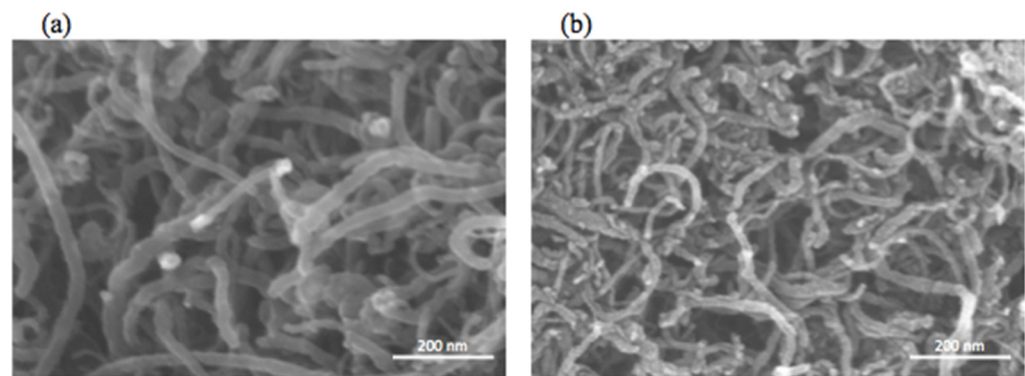
Figure 9. Scanning microscopy imaging of (**a**) SWCNT and (**b**) MWCNTs.

The fabricated composites with SWCNT and MWCNT are piezoresistive and were characterized by electrical resistance change under mechanical loading. Figure 10a shows virgin GFRP mode I critical energy release rate against separation, which is the distance between the pre-generated crack opening; Figure 10b shows load and percentage of resistance change vs. separation distance, which is the extent of separation between initial crack faces as the sample is loaded during mode I test. Time data are also included on the plot for comparison with the EM waves response data as cracks propagated throughout the specimen.
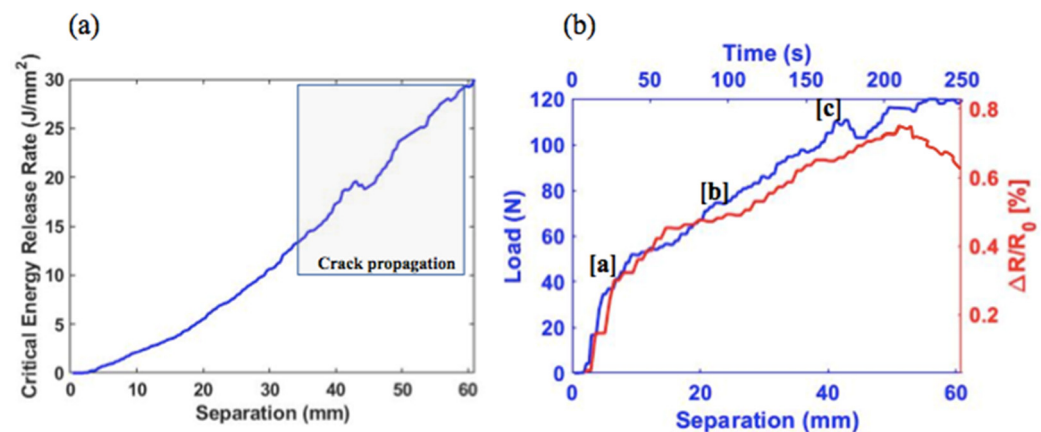

Figure 10. GFRP composite (**a**) mode I critical energy release rate, (**b**) mode I fracture propagation and percentage of resistance change where the slight charge release is labeled as [a]; upon further loading, crack propagates and more charge release was observed at both sections [b] and [c].

In virgin GFRP composites, crack initiation was observed at about 78 N. The percentage change in resistance increased during loading. As the separation increased, for every delamination observed during loading of the specimen, a change in resistance was observed, leading to a slight drop at point [c] shown in Figure 10b at higher crack separation. In GFRP composites with SWCNTs, crack propagation initiated at around 125 N with a significant increase in separation for initiation of crack propagation, as shown in Figure 11a,b.
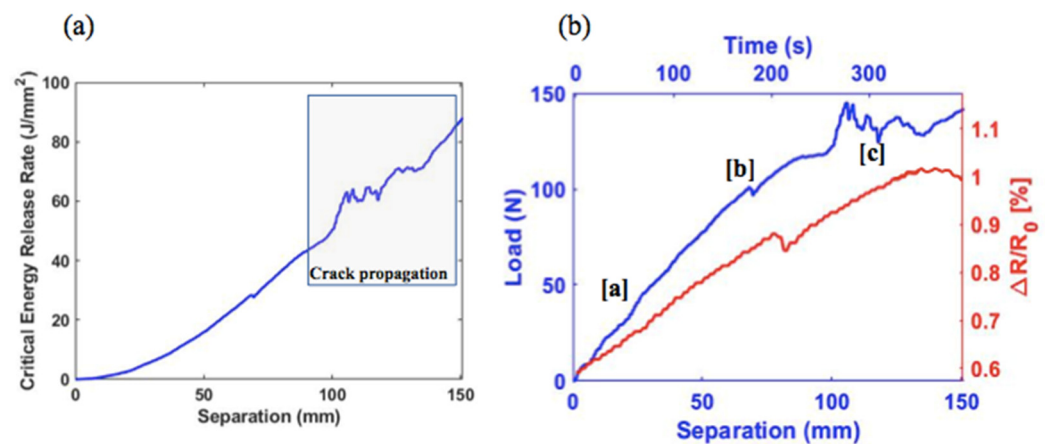
Figure 11. GFRP-SWCNT composite (**a**) mode I critical energy release rate, (**b**) mode I fracture propagation and percentage of resistance change where the slight charge release is labeled as [a]; upon further loading, crack propagates and more charge release was observed at both sections [b] and [c].

The addition of SWCNTs showed an increase in the piezoresistive property of the composite, which presented a resistance change of 0.83% at crack initiation and propagation. The data relative to the GFRP composite with MWCNTs response during mode I test are shown in Figure 12, with a peak load value of 146 N for initiation of crack propagation and followed a similar trend but lower change in resistivity to that of GFRP-SWCNT for most tested specimens. Vertuccio et al. also investigated the piezoresistive behavior of a structural resin containing a specific amount of MWCNT, measuring DC and AC resistance as well as other electrical properties when the specimens were subjected to a low number of cycles and different levels of strain loaded in both axial and flexural modes. They observed that AC measurements are more effective than DC measurements and that operating at 1 MHz improves sensitivity to sample strain. They also demonstrated that the electrical response follows the mechanical deformation in a linear fashion, both during the loading and unloading phase [24].
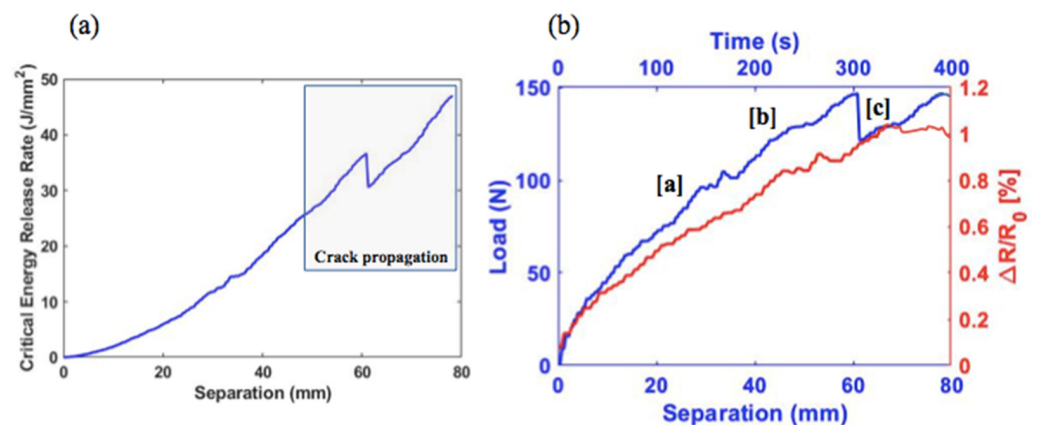

Figure 12. GFRP-MWCNT composite (**a**) mode I critical energy release rate, (**b**) mode I fracture propagation and percentage of resistance change where the slight charge release is labeled as [a]; upon further loading, crack propagates and more charge release was observed at both sections [b] and [c].

The charge released during crack propagation was collected against time. All experiments were run for the same amount of time therefore enabling the comparison of EM waves data at different time stamps with the specimen load response during separation at similar time. The response charge had noise voltage varying between −0.1 to 0.1 mV

for virgin GFRP specimens. GFRP-SWCNT composite had noise voltage varying between −0.26 to 0.26 mV, while GFRP-MWCNT specimens had noise voltage varying between −0.1 to 0.15 mV. As crack propagated through the samples, spikes in voltage amplitude were observed. The generated charge during crack propagation reached the highest value of 0.51 mV. During initial loading, the slight charge release is labeled as [a]; upon further loading, crack propagates and more charge release was observed at both sections [b] and [c], as shown in Figure 13, which plots the raw and filtered electromagnetic emitted voltage during mechanical loading. The Fourier transform was used to filter the electromagnetic emitted voltage. By filtering out random noise and identifying the frequencies associated with fracture propagation, the Fourier transform revealed crucial properties of EM waves. This was done by converting the data to a frequency domain, filtering, and converting it back to a time domain. Figure 13 shows the electromagnetic emitted voltage during mechanical loading and noise filter electromagnetic emitted voltage during mechanical loading for GFRP samples.
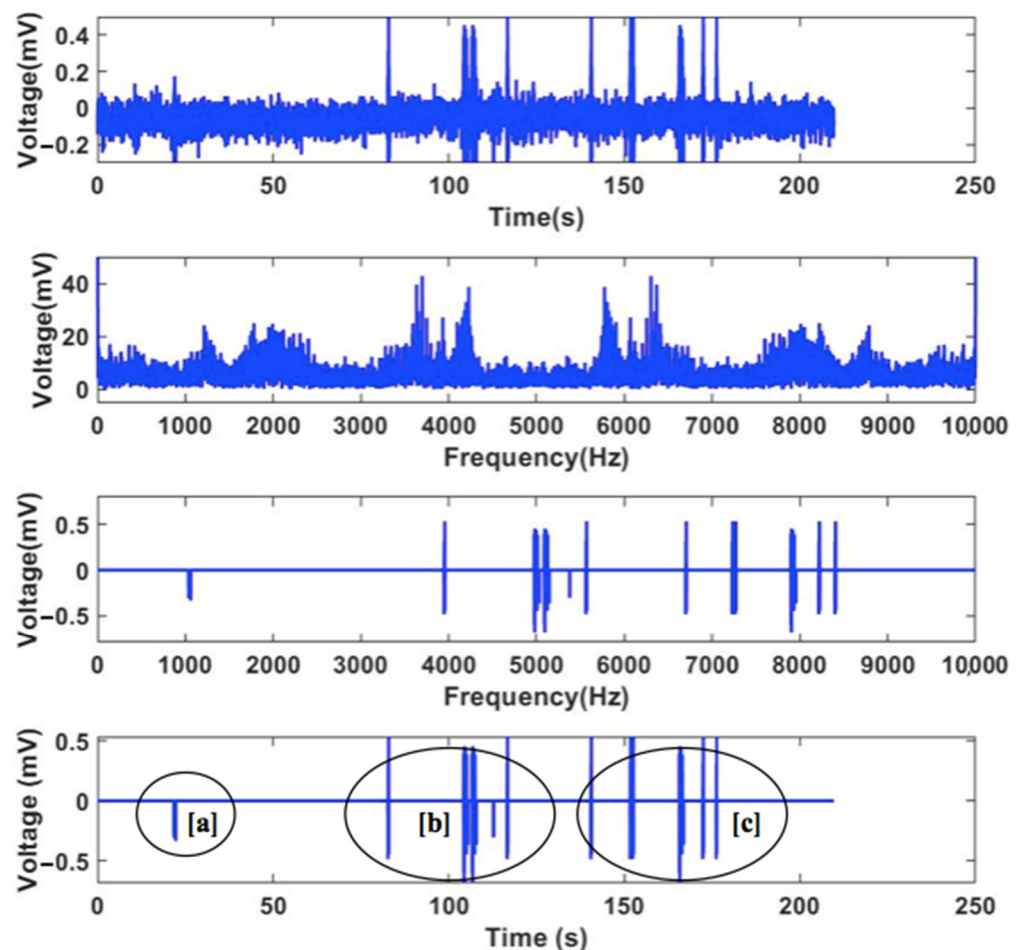

Figure 13. GFRP electromagnetic emitted voltage during mechanical loading and noise filter electromagnetic emitted voltage during mechanical loading where the slight charge release is labeled as [a]; upon further loading, crack propagates and more charge release was observed at both sections [b] and [c].

A similar trend of EM wave charge released during crack propagation was observed in [34] during the fracture of granite under compression loading. The electromagnetic emitted voltage during mechanical loading for GFRP-SWCNT before and after noise filtering is shown in Figure 14.
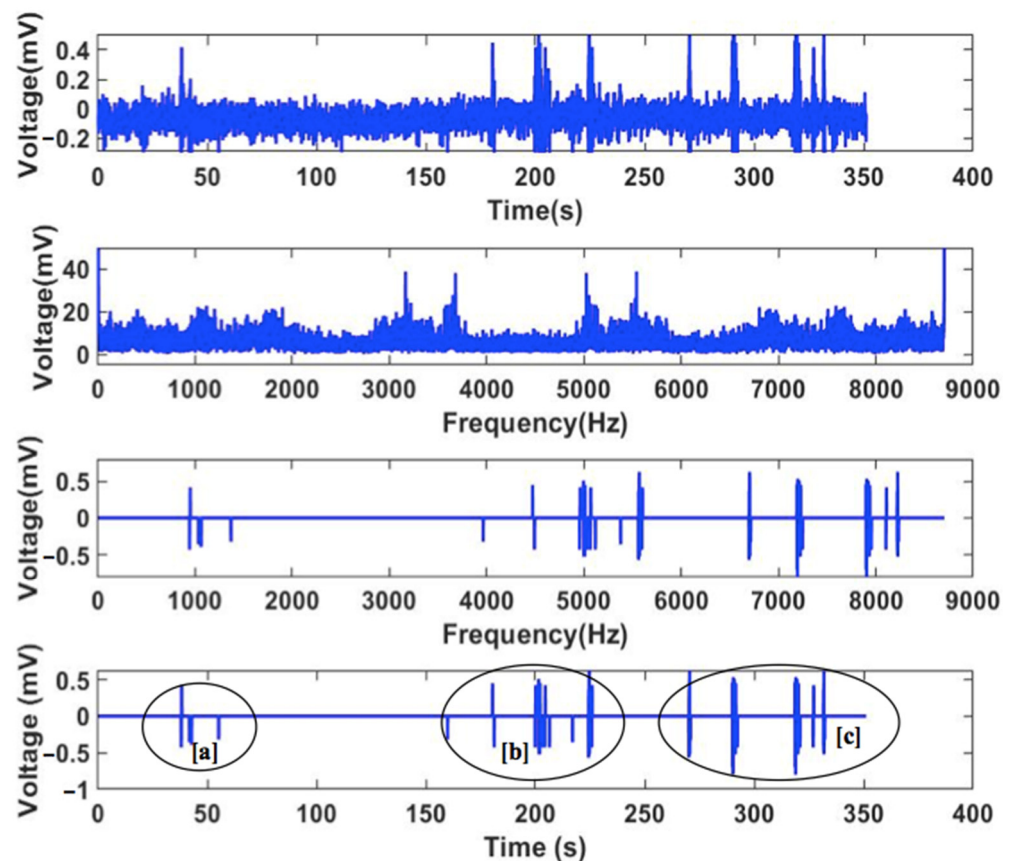
Figure 14. GFRP-SWCNT electromagnetic emitted voltage during mechanical loading and noise filter electromagnetic emitted voltage during mechanical loading where the slight charge release is labeled as [a]; upon further loading, crack propagates and more charge release was observed at both sections [b] and [c].

The generated charge during crack propagation reached the highest value of 0.52 mV. As loading proceeded at 46 s time, slight charge release was detected and labeled as [a], as shown in Figure 14. During further loading, more damage is produced as the crack propagates, and more charge release is observed at both sections [b] and [c]. Due to the improved electrical properties of the composite from the addition of SWCNTs, the electromagnetic charge emitted during the loading of the samples showed higher amplitudes. Figure 15 shows the charge emitted from the GFRP-MWCNT specimens' data. The charge released from GFRP-MWCNT samples was higher compared to the other composite types, with an amplitude of 0.53 mV. Slight jumps in released charge, as shown in Section [a], were observed at initial loading, and as loading proceeded at 210 s time, more charge release was labeled as [b] in Figure 15. When the bonds between the composite surfaces are broken and crack propagates further, more charge release was observed at section [c]. The MWCNT showed a relatively better signal response as reflected by the resistivity reported for MWCNT to be 5×10^{-6} Ω cm^{-1} [35], which was lower than SWCNT. This is likely due to MWCNTs having larger diameters and densities than typical SWCNTs [36].

The ability of the piezoresistive composite to respond to the generation and propagation of crack is demonstrated by both the resistivity response and EM emissions at the crack surface. Our study found that there is an improved electrical resistivity signal performance due to embedded CNTs into the composite. These systems enable real time detection of crack propagation from both electrical resistivity data and EM waves response. However, additional tests need to be performed to better understand the nature of EM emissions and how they can be used to detect and predict various damage modes.
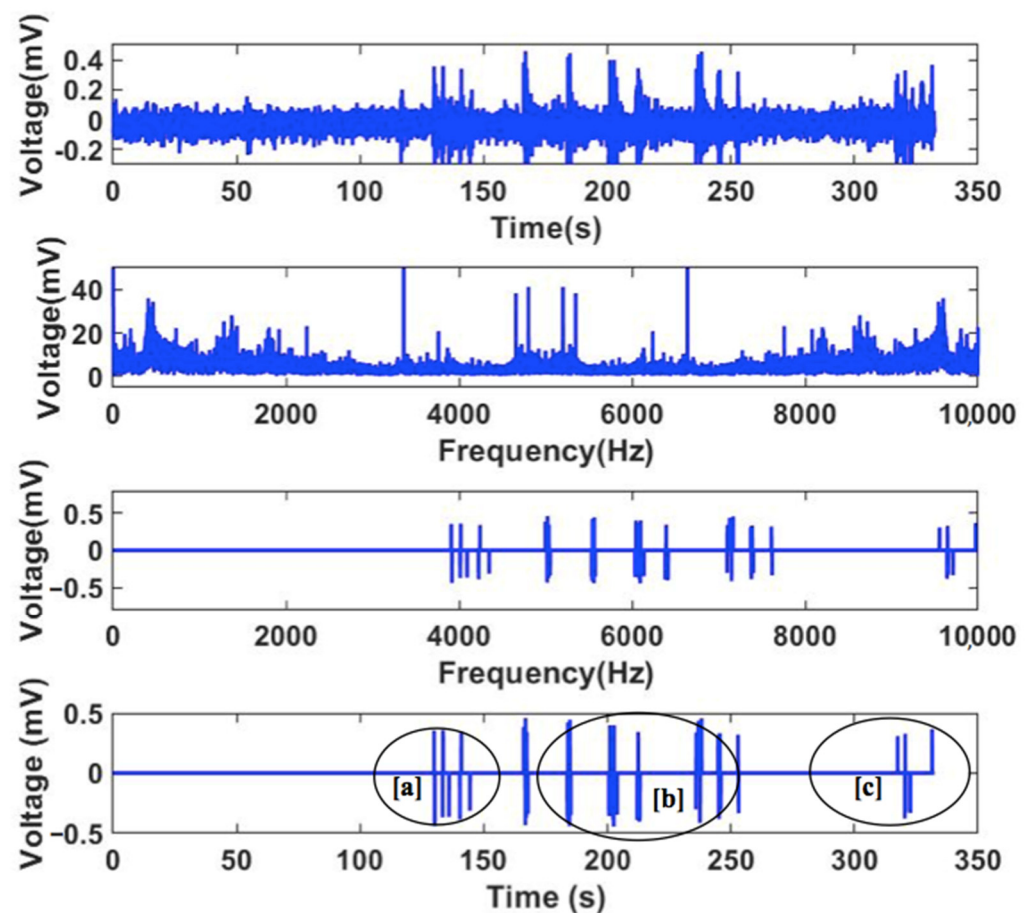
Figure 15. GFRP-MWCNT electromagnetic emitted voltage during mechanical loading and noise filter electromagnetic emitted voltage during mechanical loading where the slight charge release is labeled as [a]; upon further loading, crack propagates and more charge release was observed at both sections [b] and [c].

4. Conclusions

This work focuses on the mechanical performance of the piezoresistive composite for structural health monitoring. The synthesis of carbon nanotubes followed the chemical vapor deposition process for both the single walled carbon nanotubes and multiwalled carbon nanotubes. The characterization of the fabricated carbon nanotubes was carried out using FTIR for bond properties, DSC for thermal properties and SEM imaging to observe the surface morphology of the nanotubes. The grown nanotubes were used to fabricate piezoresistive composites with both SWCNT and MWCNTs. The relation between electrical resistance and separation during mode I tests identified together with the detection of electromagnetic charge emitted from the composite specimens as crack propagates. It was observed that specimens without nanotubes embedded have less resistivity change and emitted less charge during the damage development and morphological change. The addition of SWCNTs and MWCNTs contributed to the increase in electrical resistivity changes, which was reflected in an increase of charge released at the crack tip during its propagation. Additional testing is required to detect and predict initiation and propagation of different damage modes.

Author Contributions: Conceptualization, R.R., K.R., R.G.Q. and V.V.; methodology, R.R., R.G.Q. and M.M.R.; data curation, R.R., V.V., R.G.Q. and M.M.R.; writing—original draft preparation, R.G.Q. and M.M.R.; writing—review and editing, R.R., V.V., R.G.Q. and M.M.R.; supervision, R.R. and V.V. All authors have read and agreed to the published version of the manuscript.

References

1. Sun, M.; Staszewski, W.J.; Swamy, R.N. Smart Sensing Technologies for Structural Health Monitoring of Civil Engineering Structures. *Adv. Civ. Eng.* **2010**, *2010*, 724962. [CrossRef]
2. Kang, I.; Heung, Y.Y.; Kim, J.H.; Lee, J.W.; Gollapudi, R.; Subramaniam, S.; Narasimhadevara, S.; Hurd, D.; Kirikera, G.R.; Shanov, V.; et al. Introduction to carbon nanotube and nanofiber smart materials. *Compos. Part B Eng.* **2006**, *37*, 382–394. [CrossRef]
3. Qhobosheane, R.G.; Elenchezhian, M.R.P.; Das, P.P.; Rahman, M.; Rabby, M.M.; Vadlamudi, V.; Reifsnider, K.; Raihan, R. Smart Self-Sensing Composite: Piezoelectric and Mag-netostrictive FEA Modeling and Experimental Characterization Using Wireless Detection Systems. *Sensors* **2020**, *20*, 6906. [CrossRef] [PubMed]
4. Liu, L.; Xu, J.; Yin, T.; Wang, Y.; Chu, H. Improved conductivity and piezoresistive properties of Ni-CNTs cement-based composites under magnetic field. *Cem. Concr. Compos.* **2021**, *121*, 104089. [CrossRef]
5. Wang, Y.; Wang, S.; Li, M.; Gu, Y.; Zhang, Z. Piezoresistive response of carbon nanotube composite film under laterally compressive strain. *Sens. Actuators A Phys.* **2018**, *273*, 140–146. [CrossRef]
6. Sanli, A.; Müller, C.; Kanoun, O.; Elibol, C.; Wagner, M.F.-X. Piezoresistive characterization of multi-walled carbon nanotube-epoxy based flexible strain sensitive films by impedance spectroscopy. *Compos. Sci. Technol.* **2016**, *122*, 18–26. [CrossRef]
7. Sanli, A.; Benchirouf, A.; Müller, C.; Kanoun, O. Piezoresistive performance characterization of strain sensitive multi-walled carbon nanotube-epoxy nanocomposites. *Sens. Actuators A Phys.* **2017**, *254*, 61–68. [CrossRef]
8. Al-Sabagh, A.; Taha, E.; Kandil, U.; Nasr, G.-A.; Taha, M.R. Monitoring Damage Propagation in Glass Fiber Composites Using Carbon Nanofibers. *Nanomaterials* **2016**, *6*, 169. [CrossRef]
9. Zhou, Y.X.; Wu, P.X.; Cheng, Z.; Ingram, J.; Jeelani, S. Improvement in electrical, thermal and mechanical properties of epoxy by filling carbon nanotube. *Express Polym. Lett.* **2008**, *2*, 40–48. [CrossRef]
10. Mutlib, N.; Bin Baharom, S.; El-Shafie, A.; Nuawi, M.Z. Ultrasonic health monitoring in structural engineering: Buildings and bridges. *Struct. Control Health Monit.* **2015**, *23*, 409–422. [CrossRef]
11. Shafiee, M.; Abbas, M. Structural Health Monitoring (SHM) and Determination of Surface Defects in Large Metallic Structures using Ultrasonic Guided Waves. *Sensors* **2018**, *18*, 3958.
12. Gkantou, M.; Muradov, M.; Kamaris, G.S.; Hashim, K.; Atherton, W.; Kot, P. Novel Electromagnetic Sensors Embedded in Reinforced Concrete Beams for Crack Detection. *Sensors* **2019**, *19*, 5175. [CrossRef] [PubMed]
13. Huang, C.; Zhou, X.; Rong, K.; Cao, J.; Zhang, J.; Wang, K. Smart Coating based on Frequency-Selective Spoof Surface Plasmon Polaritons for Crack Monitoring. In Proceedings of the IEEE International Conference on Electronic Information and Communication Technology (ICEICT), Shenzhen, China, 13–15 November 2020; IEEE: Piscataway, NJ, USA, 2020; pp. 758–760. [CrossRef]
14. Abbasi, K.; Motlagh, N.H.; Neamatollahi, M.R.; Hashizume, H. Detection of axial crack in the bend region of a pipe by high frequency electromagnetic waves. *Int. J. Press. Vessel. Pip.* **2009**, *86*, 764–768. [CrossRef]
15. Mori, Y.; Obata, Y.; Sikula, J. Acoustic and electromagnetic emission from crack created in rock sample under deformation. *J. Acoust. Emiss.* **2009**, *27*, 157–166.
16. Pereira, G.F.; Mikkelsen, L.P.; McGugan, M. Crack Detection in Fibre Reinforced Plastic Structures Using Embedded Fibre Bragg Grating Sensors: Theory, Model Development and Experimental Validation. *PLoS ONE* **2015**, *10*, e0141495. [CrossRef]
17. Kwon, D.-J.; Shin, P.-S.; Kim, J.-H.; Wang, Z.-J.; DeVries, K.L.; Park, J.-M. Detection of damage in cylindrical parts of carbon fiber/epoxy composites using electrical resistance (ER) measurements. *Compos. Part B Eng.* **2016**, *99*, 528–532. [CrossRef]
18. Gonzalez, R.; Mcdonald, A.; Mertiny, P. Damage detection method for fiber-reinforced polymer composites using AL-12SI flame-sprayed coatings. In Proceedings of the International SAMPE Technical Conference, Paris, France, 10–11 March 2014.
19. Wang, D.; Chung, D.D.L. Through-thickness piezoresistivity in a carbon fiber polymer-matrix structural composite for electrical resistance-based through-thickness strain sensing. *Carbon.* **2013**, *60*, 129–138. [CrossRef]
20. Mattox, D.M. Physical vapor deposition (PVD) processes. *Met. Finish.* **2002**, *100*, 394–408. [CrossRef]
21. PlanarTech. Planargrow Graphene CVD Systems. *May 2021.* Available online: https://www.planartech.com/cvd-systems.html (accessed on 15 April 2022).
22. Kuo, D.-H.; Huang, K.-W. Kinetics and microstructure of TiN coatings by CVD. *Surf. Coat. Technol.* **2001**, *135*, 150–157. [CrossRef]
23. ASTM D5528. *Standard Test Method for Mode I Interlaminar Fracture Toughness of Unidirectional Fiber-Reinforced Polymer Matrix Composites*; ASTM: West Conshohocken, PA, USA, 2013.
24. Vertuccio, L.; Guadagno, L.; Spinelli, G.; Lamberti, P.; Tucci, V.; Russo, S. Piezoresistive properties of resin reinforced with carbon nanotubes for health-monitoring of aircraft primary structures. *Compos. Part B Eng.* **2016**, *107*, 192–202. [CrossRef]
25. Rathore, D.; Prusty, R.K.; Kumar, D.S.; Ray, B.C. Mechanical performance of CNT-filled glass fiber/epoxy composite in in-situ elevated temperature environments emphasizing the role of CNT content. *Compos. Part A Appl. Sci. Manuf.* **2016**, *84*, 364–376. [CrossRef]

26. Samson, G.; Deby, F.; Garciaz, J.-L.; Perrin, J.-L. A new methodology for concrete resistivity assessment using the instantaneous polarization response of its metal reinforcement framework. *Constr. Build. Mater.* **2018**, *187*, 531–544. [CrossRef]

27. Geddes, T.; Ragheb, L.A. Electrical properties of metallic electrodes. *Med. Biol. Eng. Comput.* **1990**, *28*, 182–186.

28. Rabby, M.M.; Rahman, M.; Das, P.P.; Elenchezhian, M.R.P.; Qhobosheane, R.G.; Vadlamudi, V.; Reifsnider, K.; Raihan, R. The Effect of Room-Temperature Aging on Enthalpy and Dielectric Property of Carbon-Fiber/Epoxy Composite Prepreg and the Mechanical Property of Manufactured Composite. In Proceedings of the SAMPE Conference 2021 Proceedings, Dallas, TX, USA, 19–21 October 2021.

29. Hsieh, Y.-C.; Chou, Y.-C.; Lin, C.-P.; Hsieh, T.-F.; Shu, C.-M. Thermal Analysis of Multi-walled Carbon Nanotubes by Kissinger's Corrected Kinetic Equation. *Aerosol Air Qual. Res.* **2010**, *10*, 212–218. [CrossRef]

30. Ozawa, T. A New Method of Analyzing Thermogravimetric Data. *Bull. Chem. Soc. Jpn.* **1965**, *38*, 1881–1886. [CrossRef]

31. Pal, A.K.; Vimal, K. Theoretical and analyzed data related to thermal degradation kinetics of poly (l-lactic acid)/chitosan-grafted-oligo l-lactic acid (PLA/CH-g-OLLA) bionanocomposite films. *Data Brief* **2017**, *10*, 304–311. [CrossRef]

32. Lin, C.-P.; Lin, J.-Z.; Shu, C.-M.; Tseng, J.-M. Multi-walled carbon nanotube thermal stability characteristics evaluation by DSC tests. *J. Loss Prev. Process Ind.* **2012**, *25*, 302–308. [CrossRef]

33. Brukha, R.; Somenath, M. Kinetics of carbon nanotubeoxidation. *J. Mater. Chem.* **2007**, *17*, 619–623. [CrossRef]

34. Frid, V.; Rabinovitch, A.; Bahat, D. Fracture induced electromagnetic radiation. *J. Phys. D Appl. Phys.* **2003**, *36*, 1620. [CrossRef]

35. Schönenberger, C.; Bachtold, A.; Strunk, C.; Salvetat, J.-P.; Forró, L. Interference and Interaction in multi-wall carbon nanotubes. *Appl. Phys. A* **1999**, *69*, 283–295. [CrossRef]

36. Lekawa-Raus, A.; Patmore, J.; Kurzepa, L.; Bulmer, J.; Koziol, K. Electrical Properties of Carbon Nanotube Based Fibers and Their Future Use in Electrical Wiring. *Adv. Funct. Mater.* **2014**, *24*, 3661–3682. [CrossRef]